

Qualitative comparative analysis of MgB₂ powder-in-tube wires: superconductivity and X-ray cone-beam microtomography

P. BADICA*, I. TISEANU^a, G. ALDICA, T. CRACIUNESCU^a, V. SANDU, G. JAKOB^b, M. RINDFLEISCH^c

National Institute for Materials Physics, 077125 Bucharest, Romania

^a*National Institute for Lasers, Plasma and Radiation Physics, Bucharest, 077125 Romania*

^b*Mainz University, Institute of Physics, 55128 Mainz, Germany*

^c*Hyper Tech Research Inc, Columbus, OH 43228, USA*

Commercial wires of MgB₂ with different architectures and two different heat treatments were characterized with respect to their superconducting properties (T_c , J_c , H_{irr} , pinning force, macro flux jumps behaviour) through magnetic measurements and were visualized by 3D x-ray micro-tomography (XRT). For a particular architecture, heat treatment conditions of 625 °C/3 hrs or 700 °C/30 min produced relatively small differences, whereas the architecture of the wires showed a strong influence on superconducting characteristics. XRT checks the integrity of the wires easily detecting in a non-invasive way 3D macro defects and shows their hidden extended shape. XRT also allows a comparative geometry analysis between similar elements (e.g. filaments or filaments-matrix interfaces) from a particular wire or from wires with different architectures. Namely, XRT shows that the *geometrical perfection* (defined as the degree of departure of the geometry from the designed one) of the inner MgB₂ filaments from the wires with 18 elements was lower than for the outermost ones from the same wires and was also lower than for the filaments from the wires with 7 elements. It is proposed that these results of geometrical perfection correlate with better overall superconducting quality of the wires with 7 filaments (except for the stronger presence of macro flux jumps in the wires with 7 filaments).

(Received February 20, 2015; accepted October 28, 2015)

Keywords: MgB₂, wires, Critical current density, Microtomography, Pinning force

1. Introduction

Superconductivity offers tremendous opportunities for the development of new applications tackling energy, fast transportation, new electronics, computing and communication, new research and medical equipment or ecology problems. One candidate for superconducting industrial applications is MgB₂. However, in this respect, MgB₂ still requires optimization of a number of critical parameters, while keeping the costs competitive. To solve such a complex multi-faceted problem, the general approach is to design and create new MgB₂-based composite materials such as composite wires or tapes with different architectures and to compare them. This allows a better understanding of the specific problems for the generation of viable solutions towards further improvements.

In this work we investigate commercial MgB₂ wires with different architecture and which were obtained by two different heat treatments. We present in a qualitative comparative manner their relative superconducting properties as they are revealed by magnetic characterization. We employ 3D X-ray microtomography (XRT) technique in an attempt to find a correlation between architecture and superconducting properties. In a previous work we have reported that X-ray tomography is a very useful tool that can provide unique information on the 3D *local density distribution* in MgB₂ bulk samples

and tapes [1] with possible implications on the functional superconducting characteristics of the samples. In this article, the architecture and architectural integrity of the wires revealed by XRT in a non-invasive and convenient way allow the observation of the degree of the *geometrical perfection* and facilitates the search for defects encountered within the composing elements of the composite wires or at the interfaces between them. We look into possibility to correlate the *geometrical perfection* and superconducting characteristics of the wires. It is worth noting that the XRT method works on extended 3D volumes, and that is a significant advantage vs. 2D SEM or optical microscopy: the 3D reconstructed XRT images can reveal hidden defects that can easily go unnoticed with traditional microscopy methods.

2. Experimental

Superconducting round wires of MgB₂ were produced by Hyper Tech Research Inc. by *in-situ* continuous tube forming and filling (CTFF) process [2]. Samples are tabulated in Table 1. We shall note that for coils applications, round-shape wires are more convenient when compared to tapes. However, the challenge for the round shape wires is the resulting inevitable 3D gradients of different properties. Architecture of the wire vs. processing should be investigated and optimized. For our

experiments we selected wires with 7 filaments (MB1, 4) and 18 filaments (MB2, 3, 5, 6, 9, 10). The 18 filaments wires were with 3 different amounts of the superconductor fraction (12, 16 and 17 %). One wire (MB7, 8) was of a mono filamentary type, but in this wire SiC was added.

Each type of wire was subject to a thermal treatment at 625 °C for 360 min (MB1, 3, 5, 7, 9) or at 700 °C for 30 min (MB2, 4, 6, 8, 10) (Table 1).

Table 1. Hyper Tech MgB₂ wires (diameter of 0.83 mm) investigated in this work: names, specifications, heat treatment conditions, critical temperature from $M(T)$ measurements, anisotropy γ and percolation p_c parameters.

Sample	% s/c	Sub No.	Mono barrier	Mono sheath	Multi sheath	Temp. (°C) / Time (min)	T_c (K) ($H = 1500$ Oe)	γ	p_c
MB1	16	7	Nb	Cu	Monel	625/360	35.1	4.292	0.244
MB4	16	7	Nb	Cu	Monel	700/30	36.05	4.513	0.303
MB3	16	18	Nb	Cu	Monel	625/360	35.03	4.278	0.281
MB2	16	18	Nb	Cu	Monel	700/30	34.9	4.250	0.323
MB5	17	18	Nb	Cu	Monel	625/360	35.1	4.292	0.148
MB6	17	18	Nb	Cu	Monel	700/30	34.6	4.190	0.287
MB9	12	18	Nb seamless tube	Cu	Monel	625/360	34.05	3.831	0.238
MB10	12	18	Nb seamless tube	Cu	Monel	700/30	33.76	3.852	0.238
MB7	20	1	Nb	Monel	-	625/360	32.55	4.170	0.252
MB8	20	1	Nb	Monel	-	700/30	32.68	4.0335	0.2610

Note: Starting composition was (Mg_{1.1}B₂). Samples MB7, 8 were added with 5 % at. of SiC (30 nm).

Magnetic characterization was performed on samples of ~ 2.3 cm in length using a MPMS (Quantum Design) magnetometer. In order to exclude the non-MgB₂ contribution, we measured green-un-reacted wires and a wire made of Monel. Non-MgB₂ contribution was subtracted from the $m(T)$ and $m(H)$ curves taken on the superconducting wires. Because the screening [3] effects and thermal influence [4] of the non-MgB₂ components of the wires can be significant and can generate misleading results, the absolute values of our superconducting characteristics should be regarded more as relative rather than absolute. However, considering the same methodology applied for the characterization of the wires, a qualitative analysis between the wires based on these relative values of the superconducting characteristics is thought pertinent [3]. Contribution of Nb was observed below 9 K and at low fields. At higher fields, the critical field of Nb is exceeded, and, thus the superconductivity of Nb is suppressed. Critical current density J_c was extracted from the magnetization M vs. field H loops in the temperature range 2.5-30 K, with the field applied along the wire axis. After corrections as mentioned above, J_c was determined from the irreversible magnetization ΔM using the Bean [5] relationship: $J_c = 30 \Delta M/D$, with D the average diameter of a superconducting filament.

The X-ray tomographic experiments were performed on our cone-beam X-ray tomography facility [6, 7]. The system is equipped with a high performance Nanofocus X-Ray source for non-destructive inspection with sub-micron feature recognition. The source is operational in micro- or nano- focus mode, at a tube voltage up to 225 kV and a maximum power of 10-20 W. X-Ray images can be acquired by using three different high resolution

detector types: Image Intensifier (768x576 pixels of 132x132 μm^2) for rapid non-destructive examinations and CMOS flat panel (pitch size 48 μm) as 2D imaging detectors and a line detector (pitch size 400 μm) for slice by slice scanning of high density samples. Positioning and turning around of the sample are ensured by a set of seven high precision motorized micrometric manipulators. Automation, control and data acquisition were obtained by means of an in-house software package. The tomographic reconstruction for the cone-beam scanning is based on an optimized implementation of the modified cone beam filtered back-projection algorithm. Using a parallelization technique on multiprocessors workstations, experimental data consisting of several hundreds of large radiographic images (1220x1216 pixels) are processed for building the 3D reconstructions of typically 1024x1024x1024 voxels in less than 12 min.

Scanning electron microscopy (SEM) images on fractured or polished wires were obtained with a SEM Quanta Inspect F microscope.

3. Results and Discussion

In Fig. 1 are presented the zero-field-cooling (ZFC) data of normalized magnetization as a function of temperature. The critical temperature T_c values, taken as the onset of the superconducting transition, are shown in Table 1. The wires MB1, 4 with the same architecture composed of 7 filaments show the highest T_c . Intermediate values of T_c were found for the wires with 18 filaments. Among the wires with 18 filaments the lowest values of T_c are for the wires MB9, 10 with the smallest superconductor fraction in the wire (12 %) and containing

a Nb seamless tube barrier. One observes that for a certain architecture, i.e. with 7 filaments or 18 filaments, the heat treatment influences T_c in a different manner. For the wires with 7 filaments, a heat treatment at 700 °C for 30 min leads to a higher value of T_c as compared to a treatment at 625 °C for 360 min, while for the wires with 18 filaments we got the opposite effect. This can be understood considering that a different architecture will have a different behavior during mechanical processing of the wire and, further, during the thermal treatment because the defects, crystal quality, residual stress, interdiffusion, local density and connectivity of MgB₂ are affected. The relationship between architecture, mechanical processing, thermal treatment and superconducting properties is complex and requires careful and significant further research.

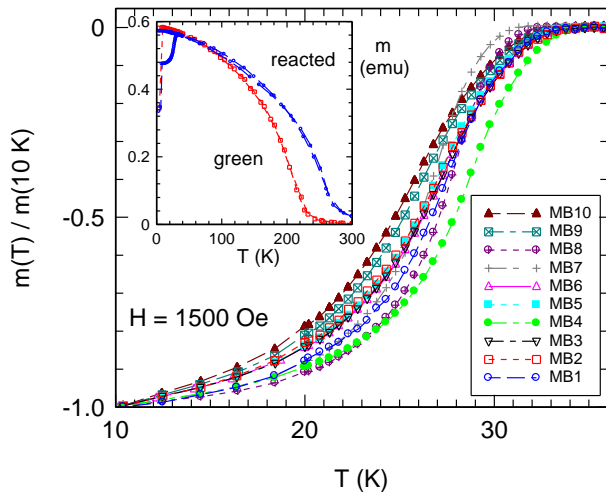


Fig. 1 Zero-filled-cooled (ZFC) normalized $M(T)/M(10\text{ K})$ curves taken for a field of 1500 Oe after subtraction of the non superconducting contribution. Inset shows as-measured ZFC and field-cooled (FC) curves for MB1 wire before (green) and after heat treatment (625 °C for 360 min).

The lowest T_c values are for the monofilamentary wires MB 7, 8. The result is normal because it is well established that SiC addition supplies C for B substitution in MgB₂ [8], but the cost is the decrease of T_c .

Apart from the T_c values, the inspection of the transition of the normalized (ZFC) magnetization indicates that between samples there are some differences. They are the consequence of the above indicated complex relationship, where the architecture of the wire is playing an important role. Since it is impossible to separate effects, a deeper analysis is not feasible. However, it can be observed that the sharpest transitions are for the monofilamentary wires MB8 and 7 followed by the 7 filaments wires MB4, 1 and finally the 18 filaments wires. The widest transitions are for the 18 filaments wires MB9 and 10.

Wires MB1 and 4 with 7 filaments show the largest difference in T_c and in the ZFC curves location vs. temperature. This may suggest that, for this architecture, the heat treatment has the strongest influence.

An interesting observation is about the magnetic behavior (Fig. 1 inset) of the non-superconducting components: for a given architecture, ZFC- $m(T)$ curves for the wire in a green or heat treated state are quite different above 100 K. A heat treatment at 700 °C for 30 min moves the $m(T)$ curve to higher values of magnetization (this is significant above 100 K) than for the heat treatment at 625 °C for 360 min (not shown). This is due to the change in the magnetic response (especially of Monel alloy) as a consequence of the work hardening and recrystallization processes during mechanical processing and thermal treatment of the wires.

Fig. 2 shows the field dependence of the critical current density J_c for each sample at several temperatures. As a general rule, the heat treatment at 700 °C for 30 min is beneficial only for the sample with 7 filaments (compare MB1 with 4). Considering the T_c data, it appears that J_c has an inverse correlation with T_c vs. heat treatment: when T_c is decreasing J_c is increasing. For a specific architecture and measurement temperature, in most cases, heat treatment is shifting the $J_c(H)$ curves in a parallel manner (compare $J_c(H)$ curves with open and closed symbols). The size of shift is different depending on the wire architecture. The highest one is obtained for the architecture with 7 filaments, i.e. wires MB1 and 4. This correlates with the largest differences in T_c and in $m(T)/m(10\text{ K})$ behavior from Fig. 1 for the same wires.

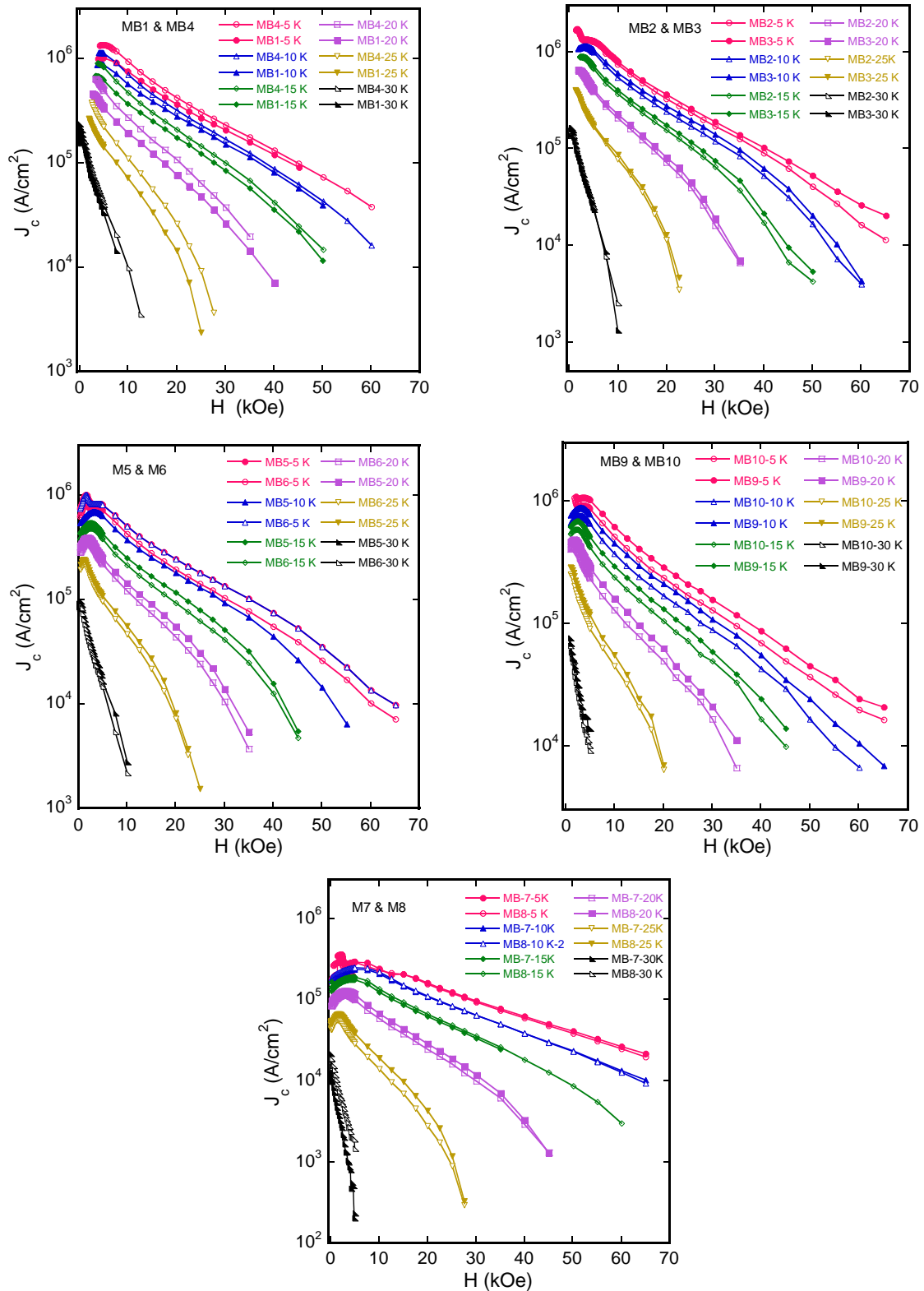


Fig. 2 Critical current density vs. magnetic field at different temperatures and for different wires. Open and filled symbols are for the wires heat treated at 625 °C for 360 min and at 700 °C for 30 min, respectively.

In Figs. 3 and 4, $J_c(H)$ curves are plotted for different heat treatments at constant temperature. For the 625 °C/360 min treatment, the order of the $J_c(H)$ increase is approximately MB5, 9, 3, 1 at all temperatures. The

increase order of $J_c(H)$ is not accompanied by an obvious T_c relationship (see Table 1). The homologous wires which were heat treated for 700 °C/30 min show, for the $J_c(H)$, the same increase order vs. architecture: MB6, 10, 2, 4. As

for the previous heat treatment, the correlation with T_c is not supported. The monofilamentary wires added with SiC, MB7 and 8, show suppressed J_c at low fields vs. the other samples, but due to a smaller slope, they are superior to the other samples at high fields. In this case the effect of SiC addition is strong and for these samples we have to consider this aspect. The scattering of the $J_c(H)$ values

among different wires (not considering the SiC added wires) is slightly higher when wires are produced at 700 °C/30 min (Fig. 4) than for 625 °C/360 min (Fig. 3). This might be related to the presence of the liquid phase usually detected above 650 °C [9].

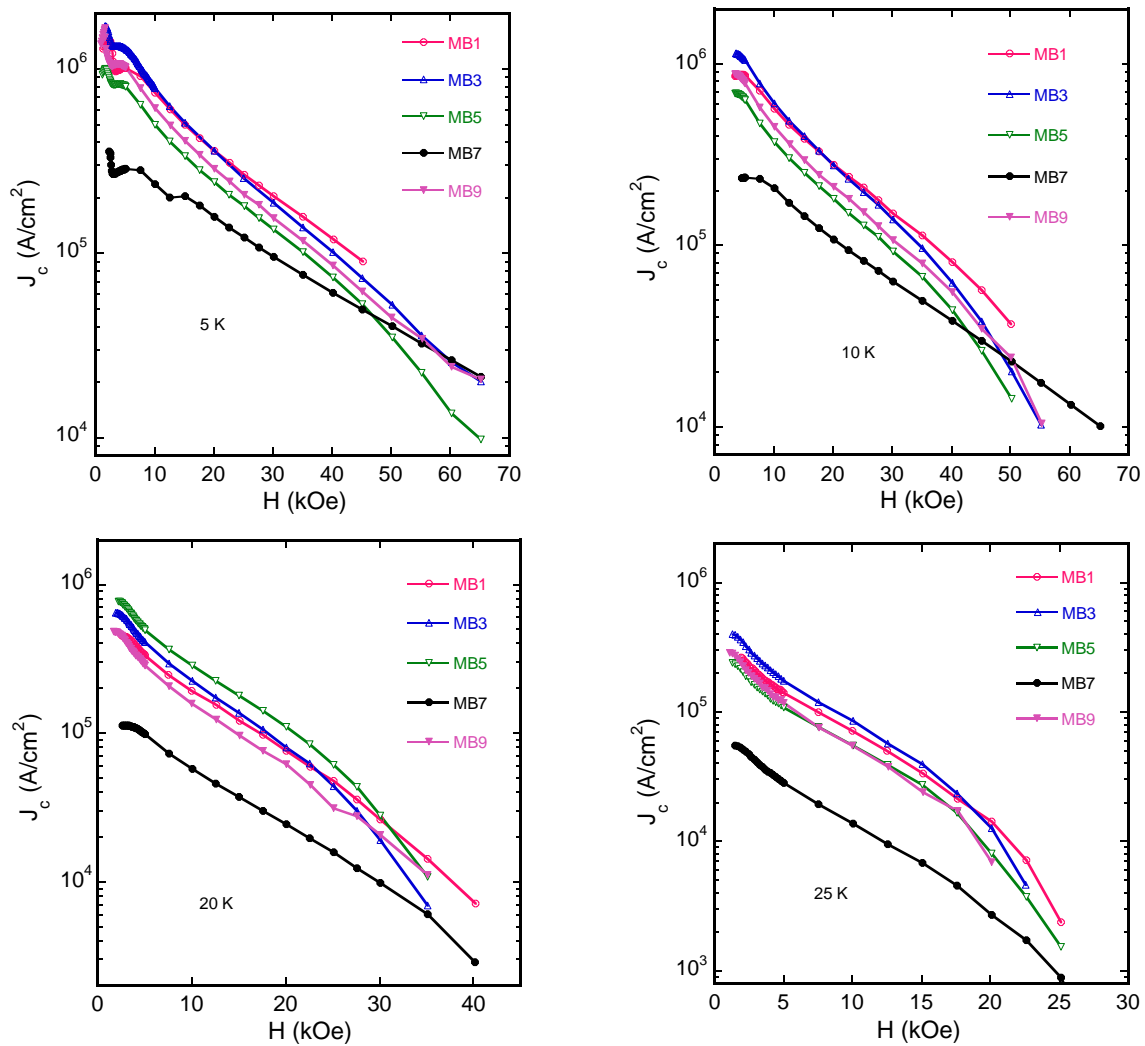


Fig. 3 Critical current density for samples heat treated at 625 °C for 360 min.

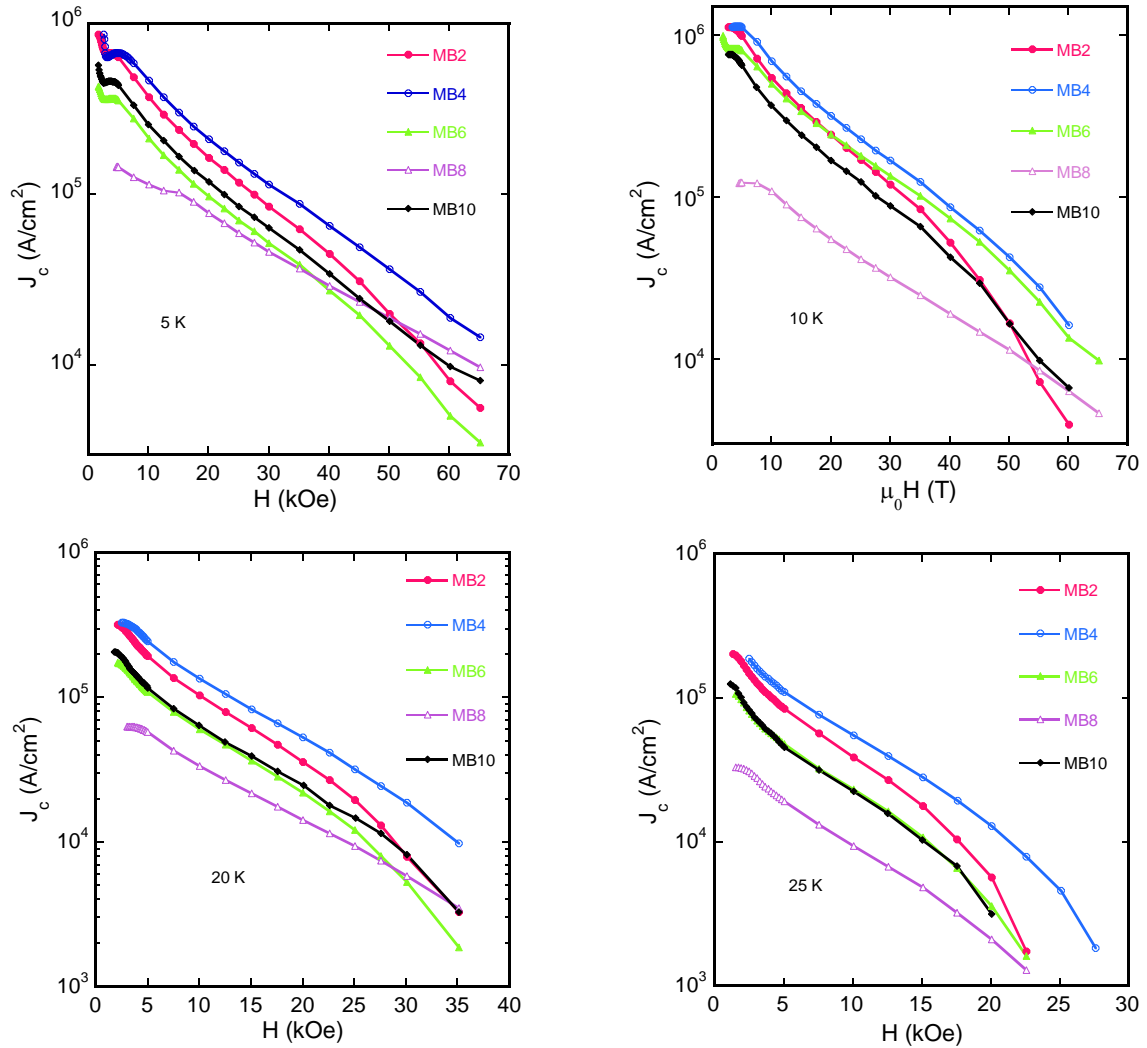


Fig. 4 Critical current density for samples heat treated at 700 °C for 30 min.

To have a closer look on the pinning behavior differences between wires we applied the 3D scaling law $F_p(x) = K(x,y,z)f(x)$ [10] where K is the scaling prefactor, proportional to the maximum value of the pinning force $F_{p, \max}$, $f(x)$ is the pinning force scaling function, and x , y , and z are the scaling variables. After Fitz and Webb, $F_p(x) = CH_{c2}^\delta(T)h^p(1-h)^q$ [11], with reduced field $h = H/H_{c2}$, and H_{c2} being the upper critical field. Variables p and q are taken temperature independent in order to preserve the shape invariance of the F_p-H curve. Results of scaling at 5 and 20 K are shown in Fig. 5 and important details are revealed. For each wire, the maximum of the pinning force scaling curves are located closer to the values $h_{\max} = 0.2$ or $h_{\max} = 0.33$ when measured at 5 and 25 K, respectively, but without matching them. Results of scaling at intermediate temperatures between 5 and 25 K bring intermediate h_{\max} values (not shown). The current situation suggests that different pinning mechanisms occur. Fitz and Webb's relationship would be correct if there is only one dominant pinning mechanism. Then, the

exponents would give information about it. For example, in the case of the pinning on grain boundaries in isotropic samples ($p = 1/2$, $q = 2$), the scaled pinning force reaches a peak for a reduced field $h_{\max} = 0.2$ while for pinning on point like defects ($p = 1$, $q = 2$) the maximum locates at $h_{\max} = 0.33$. But, when several mechanisms are acting on equal footing, or, when their weight is temperature dependent, it is quite difficult to establish a scaling procedure. Furthermore, Eisterer [12] has shown that the position of the peak of the pinning force depends also on the anisotropy factor γ and on the percolation threshold p_c . An increased γ shifts the h_{\max} to lower values with the factor $[(\gamma^2-1)p_c^2 + 1]^{-1/2}$ [12], and an increased p_c moves it to higher fields. The anisotropy factor γ (Table 1) can be estimated from T_c of the samples (Table 1) using the relationship [10]: $\gamma(T_c) = [t_c^2 + 16.7 t_c (1 - t_c)] / [3.88 - 3.724 t_c]$, with $t_c = T_c/T_{c0}$, and $T_{c0} = 39.43$ K. Introducing γ into shift factor $[(\gamma^2-1)p_c^2 + 1]^{-1/2}$ and making it equal to the experimental value of h_{\max} we can extract the percolation

threshold p_c (Table 1). We have used for this aim the data at 5 K where it is expected that the fundamental mechanism is acting without any contribution from the grains whose orientations relative to the field drive them in normal state. Since γ is directly related to T_c it will show the same tendency vs. heat treatment or architecture as T_c . This fact has already been discussed above. Here, we just observe that the percolation threshold p_c increases (or is constant for MB9, 10 wires) after the high temperature treatment (700 °C/30 min) which suggests a decrease of connectivity. The shift of h_{max} toward higher values (see

Fig. 5) with increasing temperature suggests that additional contributions come to play a significant role at high temperatures. The most probable mechanism consistent with this shift would be the pinning on point defects. It results that the high temperature heat treatment, i.e., 700 °C/30 min, promotes the pinning on point defects at high temperatures and a lower connectivity in the wires, apparently through the change to a liquid phase formation and sintering mechanism.

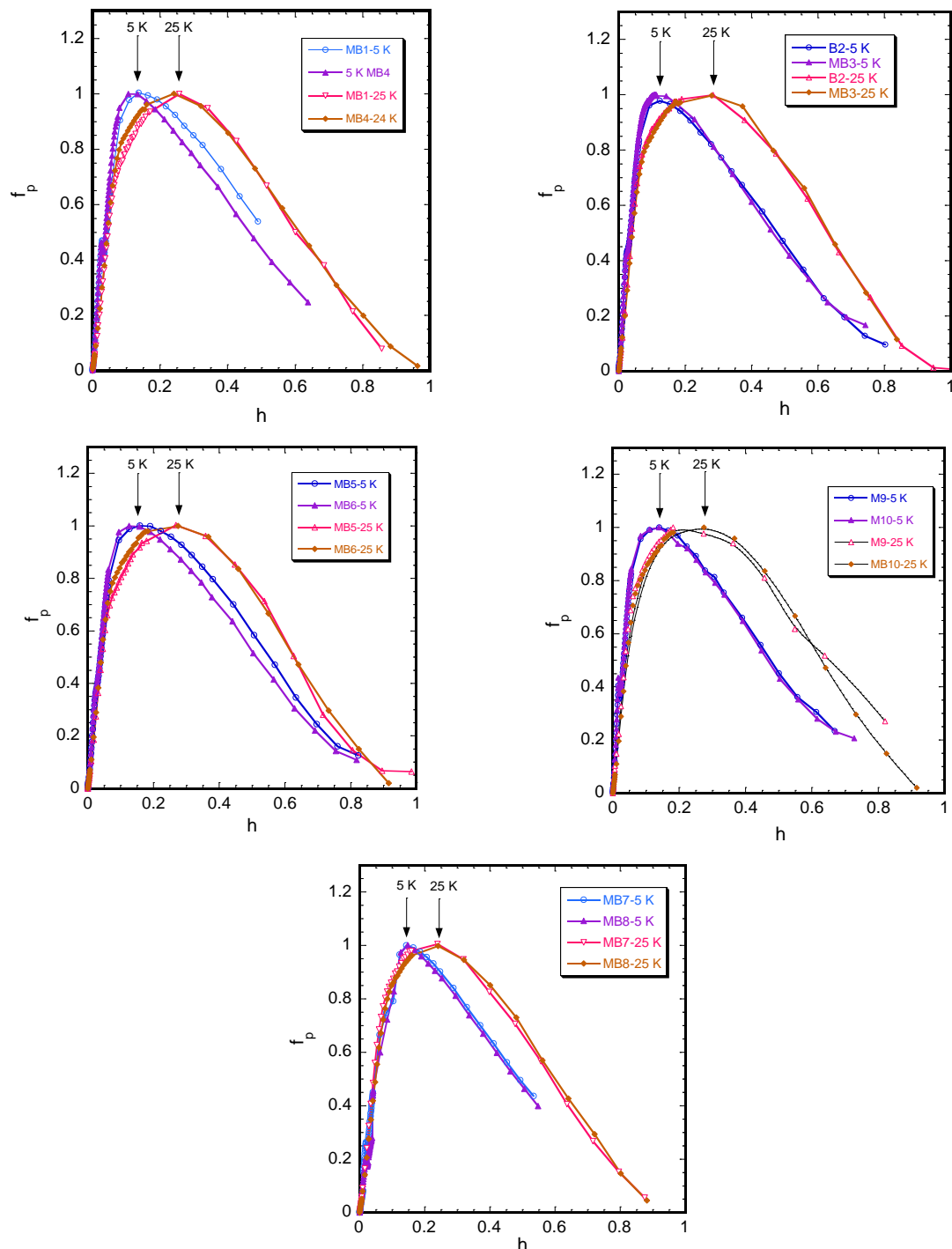


Fig. 5 Scaling of the pinning force at 5 and 25 K (reduced field of the maximum, h_{max} at 5 and 25 K is indicated with arrows).

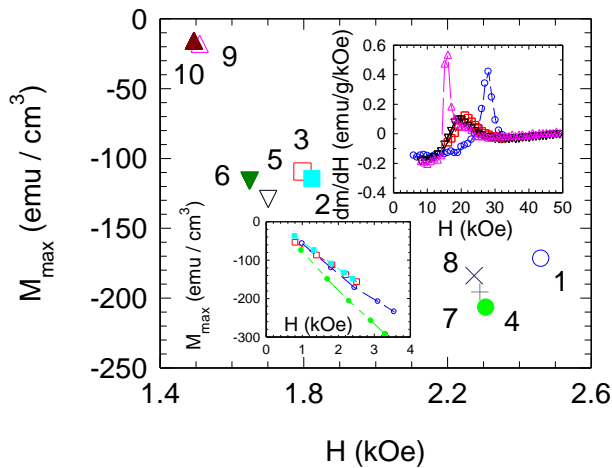


Fig. 6 Volume magnetization at the maximum of the main jump peak, M_{\max} from the first quadrant vs. magnetic field location of the peak and at 5 K. Numbers denote wires and notation is as in Table 1. Down inset shows volume magnetization M_{\max} vs. magnetic field location of the peak for the wires MB1, 2, 3 and 4 (marks are as in the main panel) for temperatures 7.5 (smaller fields), 6.25, 5, 3.75 and 2.5 K (higher fields). Upper inset shows the flux jump rate vs. position of the jump for the wires heat treated at 625 °C/360 min.

At temperatures below 10 K all samples show at least one flux jump in the first quadrant of the magnetization loops, $m(H)$. According to ref. [13], a higher J_c leads to observation of the jump at a higher field as for samples MB1, 4 (Fig. 6 main panel). Often, a few additional smaller jumps located at fields higher than the first one may occur for the samples with high J_c . In our case, a second jump was detected for samples MB1 and 4 at 5 K. A third jump is detected at 2.5 K for the sample MB 4. Heat treatment does not show a significant influence on the jumps except for the samples MB1 and 4 (the main panel of Fig. 6 and the down inset). The difference between the jump curve shape and amplitude for the two latter wires is getting smaller with the increase of the temperature. The slope of the curve for the peak of the jump $M_{\max}(H)$ vs. temperature is higher for MB4 than for MB1 as can be seen in the lower inset to Fig. 6. The slope for MB1 is slightly higher than for the wires MB2 and MB3. Among the samples with 18 filaments, wires MB2, 3, 5, 6 are not so different in terms of M_{\max} of the jump, while MB 9 and 10 are quite different. This fact suggests that not only J_c is influencing M_{\max} , but also the architecture of the wire through its thermal features might contribute: we remind that MB9 and 10 contain a rather small volume fraction of the superconducting material (12 % vs. 16 % or 17 % in the MB2, 3 and MB5, 6 wires) and the barrier is from Nb seamless tube. These elements are perhaps the reason for the noted behavior. The different behavior in the field dependence is also observable from the jump rate intensity dm/dH (upper inset to Fig. 6). Jump rate intensity is much lower (about 4 times) for the MB2, 3, 5 and 6 wires with 18 filaments

than for the other samples. Jump rate intensity is high for the wires MB1 and 4 with 7 filaments showing the highest level of J_c and T_c and it is also high for the wires MB9 and 10 composed of 18 filaments but representing a low superconducting volume fraction (12 %). Present data are not enough to propose a specific dependence between architecture, J_c , and the features of the jumps in order to further control/remove the jumps that are undesirable in practical applications.

Irreversibility fields H_{irr} extracted from Kramer plots are presented in Fig. 7. The heat treatment produces almost no influence on H_{irr} when a particular architecture is selected. A hierarchy however can be established. The highest values at 5 K are for the SiC added samples. The second best samples are the wires MB1 and 4 with 7 filaments. The lowest values are for the wires MB5 and 6, but they are not very different from the values for MB9 and 10. In fact, this quantity approximately follows the established hierarchy for J_c .

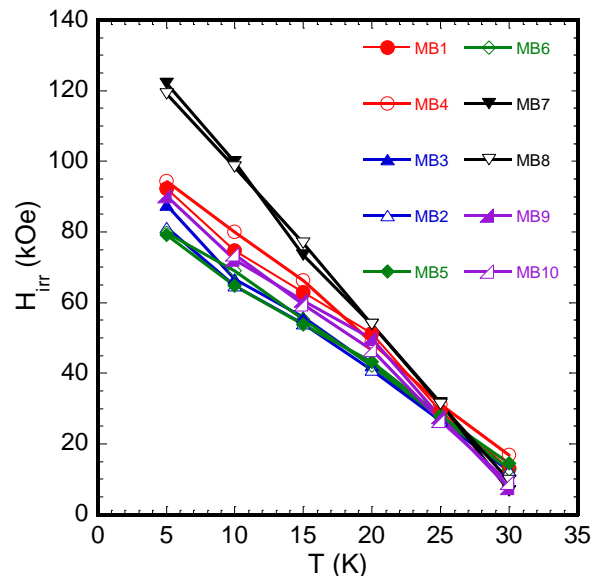


Fig. 7 Irreversibility field extracted from Kramer scaling.

Results on T_c and J_c for the non-added wires indicated that, for a given architecture, thermal treatment is influencing T_c and J_c and between them there is a direct inverted relationship, while, when a heat treatment is selected, the architecture of the wire influences T_c and J_c and no relationship between them is found.

Lack of a J_c - T_c relationship for different wire architectures when the heat treatment is constant is explained by the following:

- The architecture can have a direct effect through the geometrical perfection. For example, the negative effect of the filament “sausaging” on J_c is well known, while T_c values remain less sensitive. This effect is strong for Bi-Sr-Ca-Cu-O superconducting wires and tapes and it was considered to be a consequence of the mechanical processing instabilities that are dependent on the architecture of the composite wire [14].

- There is also an indirect influence of the architecture. As we have already mentioned, different architectures display different response to the constant conditions of mechanical processing and thermal treatment. As a result, both T_c and J_c are influenced. In this case one has to consider the MgB_2 crystal quality, defects and residual strain occurrence, recovery, distribution and so on vs. architecture and processing.

The direct and indirect influences are combined and there are 4 situations (Table 2). The probability P that the geometrical perfection of the wire should be good follows the order $P_a > P_b > P_c > P_d$. Roughly considering our T_c and J_c data, we can ascribe to situations (a)-(d) the most appropriate architectures: for (a) would correspond wires with 7 filaments, for (b, c) the wires with 18 filaments and for (d) the wires with 1 filament. However, the judgment for the wire with 1 filament might not be true because this wire contains addition of SiC to MgB_2 . It results that the geometrical perfection at least for the wires with 7 filaments is expected to be better than for the wires with 18 filaments. To observe the geometrical perfection and defects in the wires we used 3D X-ray microtomography (XRT). We show that XRT is a useful method that reveals enhanced and valuable information comparative to SEM or optical microscopy.

Table 2. Correlation between J_c and T_c of the wires and their geometrical perfection.

Situations	\uparrow =high; \downarrow =low	Expectations	Possible most appropriate wires
(a)	$J_c \uparrow, T_c \uparrow$	The highest probability P_a that geometrical perfection is good	Wires with 7 filaments
(b)	$J_c \uparrow, T_c \downarrow$	Intermediate probability P_b that geometrical perfection is good	Wires with 18 filaments
(c)	$J_c \downarrow, T_c \uparrow$	Intermediate probability P_c that geometrical perfection is good	Wires with 18 filaments
(d)	$J_c \downarrow, T_c \downarrow$	The lowest probability P_d that geometrical perfection is good	Wires with 1 filament

Typical SEM images are presented in Fig. 8. The images a) and b) show a general view of the transversal cross section for the wire MB1 with 7 filaments and there are no special details. On the other hand, images taken with secondary electrons and back scattering modes on polished transversal (Fig. 8c and d) and longitudinal (Fig. 8e and f) cross sections point to possible imperfections and defects located at the interface of the superconducting regions with the other materials; some interfaces are showing high roughness (indicated with continuous arrows) while others are straight lines (interrupted arrows). The other MgB_2 wires show similar features (data not shown). We note that SEM 2D images taken on randomly selected cross sections are not enough to perform a comparative analysis between different wires. It is necessary to observe the 3D architecture of the wire and to compare the geometrical perfection. One can define *geometrical perfection* as the degree of departure of the geometry from the ideal designed geometry. Especially important is this parameter for the superconducting filament, but also for the other components of the composite wire. Geometrical perfection of a filament includes the roughness of the interface. A special attention should be given to the search and observation of micro defects compromising the integrity of the filament or of the wire such as voids which can produce significant or full reduction of the filament cross section available for the current path.

The 3D XRT can easily detect voids. Low density characteristics of a void means that it will appear as black colour on the XRT images. An example of a void fully interrupting the Nb barrier material for the same MB1 wire is shown in Fig. 9. The void is quickly found by looking in the XRT at the transversal cross sections taken at a certain step along the length of the wire (Fig 9b). The void defect can be better observed in the longitudinal cross section from Fig. 9c. A second longitudinal cross section (Fig. 9d) taken at 90° with respect to the first one (Fig. 9c) shows that in fact the void has an extended shape, which is otherwise hidden at the first fast examination. Another important observation is that the geometrical perfection is worse for the inner filament than for the outer ones (for the inner filament roughness of the interface is higher and the ‘diameter’ fluctuations along the length are higher).

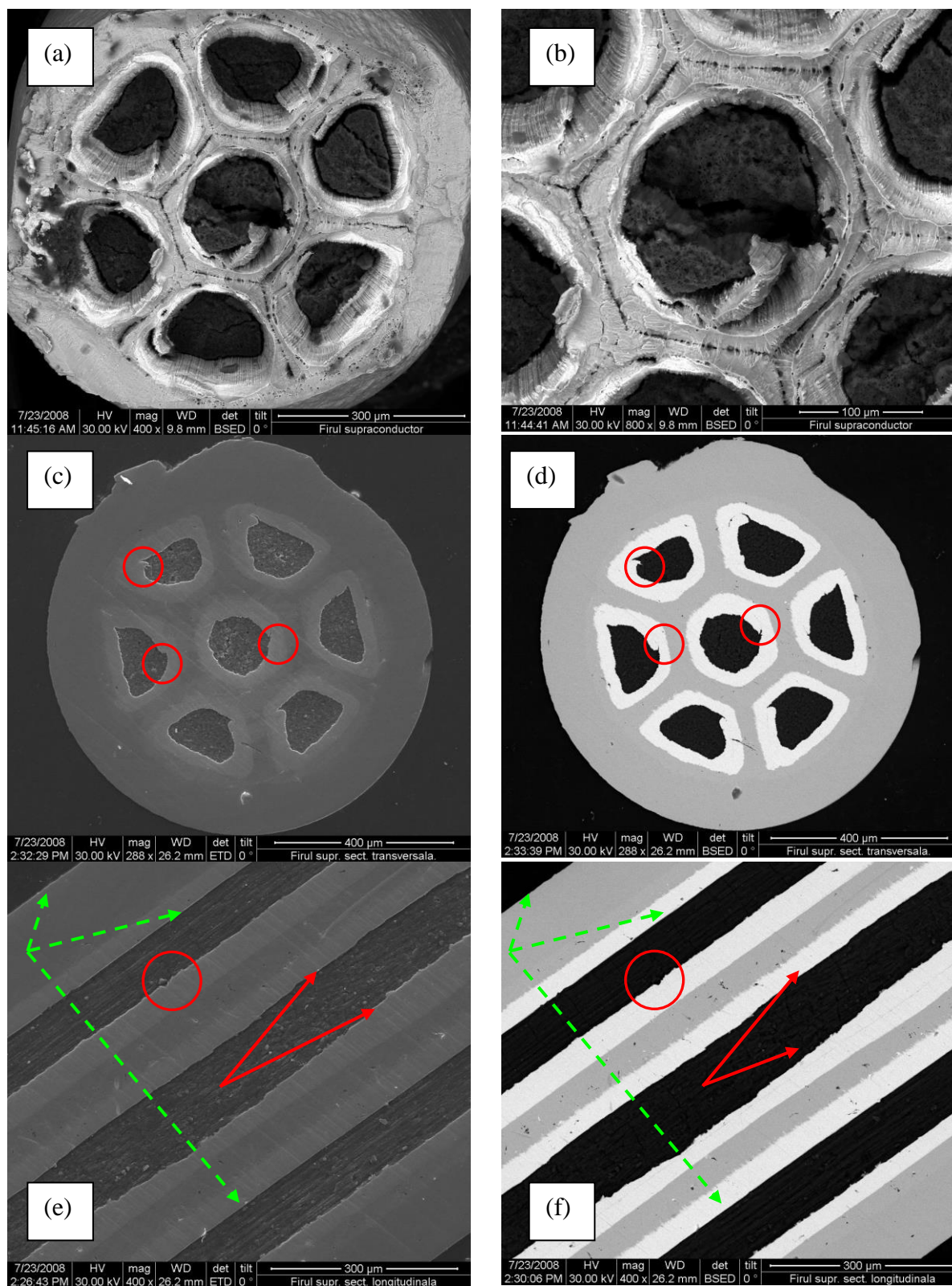


Fig. 8 SEM images of the MgB_2 wire MB1. Images a) and b) show the cross section and a detail on a fractured surface. Images c) and d) are the cross section and e) and f) are the longitudinal section revealed on polished surfaces. Images c), e) and d), f) were taken in the secondary electrons (SE) and backscattering (BSE) regimes, respectively. Circles and arrows with continuous line indicate possible defects or interfaces between the component materials with defects. Arrows with interrupted line point on apparently smooth and defects-free interfaces.

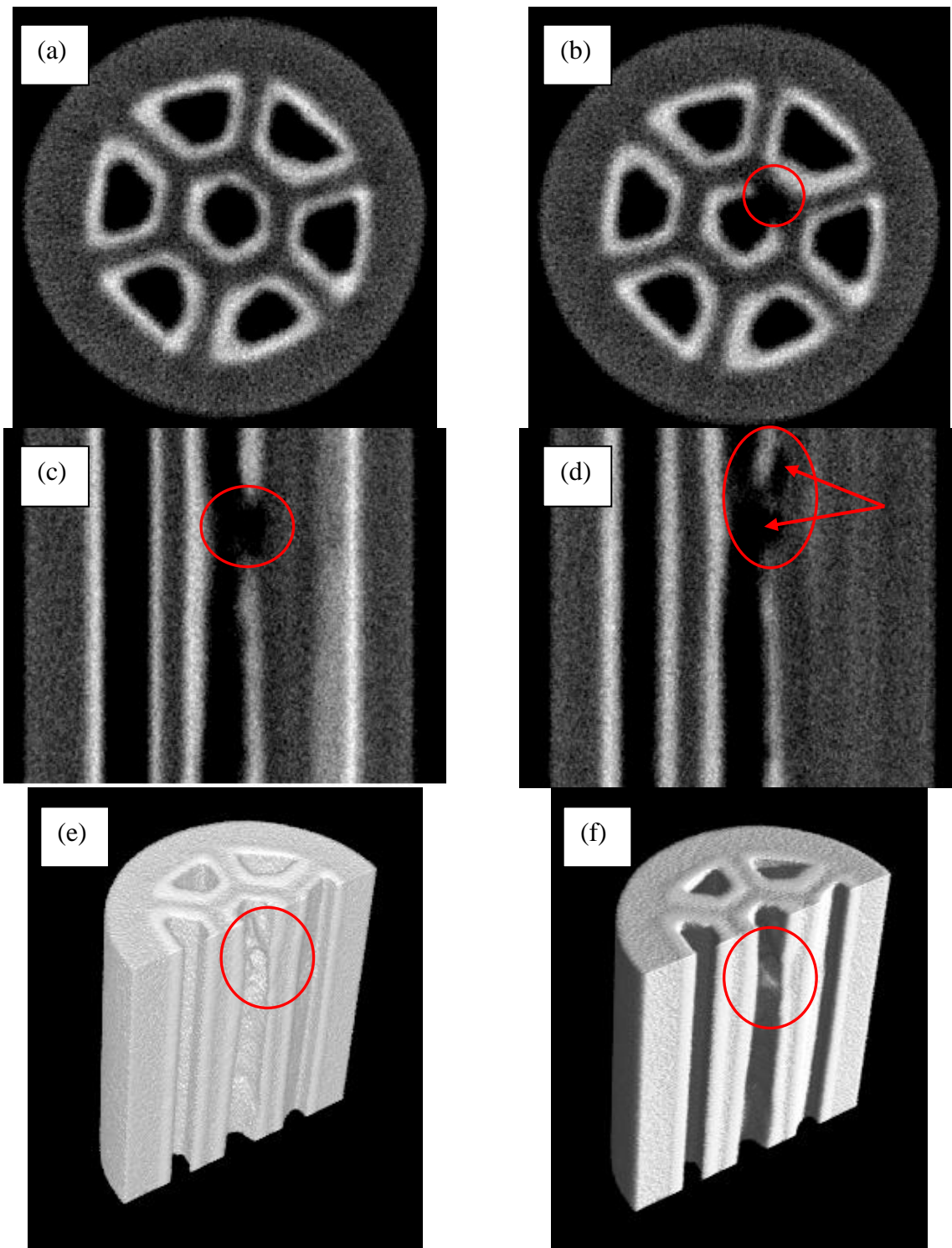


Fig. 9 X-ray microtomography images of the Hypertech MgB₂ wire MB1: a)-axial, b)-axial showing a defect, c)-sagittal showing the same defect, d) frontal showing the same defect: note that the defect is an extended one (arrows), e) and f) are 3D reconstructions for different processing conditions of the images showing the same defect and some other details (see text).

Figs. 10 and 11 show XRT images for wires MB3 and MB2 with 18 filaments, respectively. Heat treatment does not induce significant differences in the geometrical quality of the two wires. As for the 7 filament wire there are differences in the geometrical perfection between the inner and outer filaments and a lower perfection is for the inner ones. It is also easy to observe that the 18 filaments

wires have a lower geometrical perfection (especially for the inner filaments) than for the 7 filaments wires. This is consistent with the above discussion. The geometrical perfection of the wires with one filament and added with SiC is low.

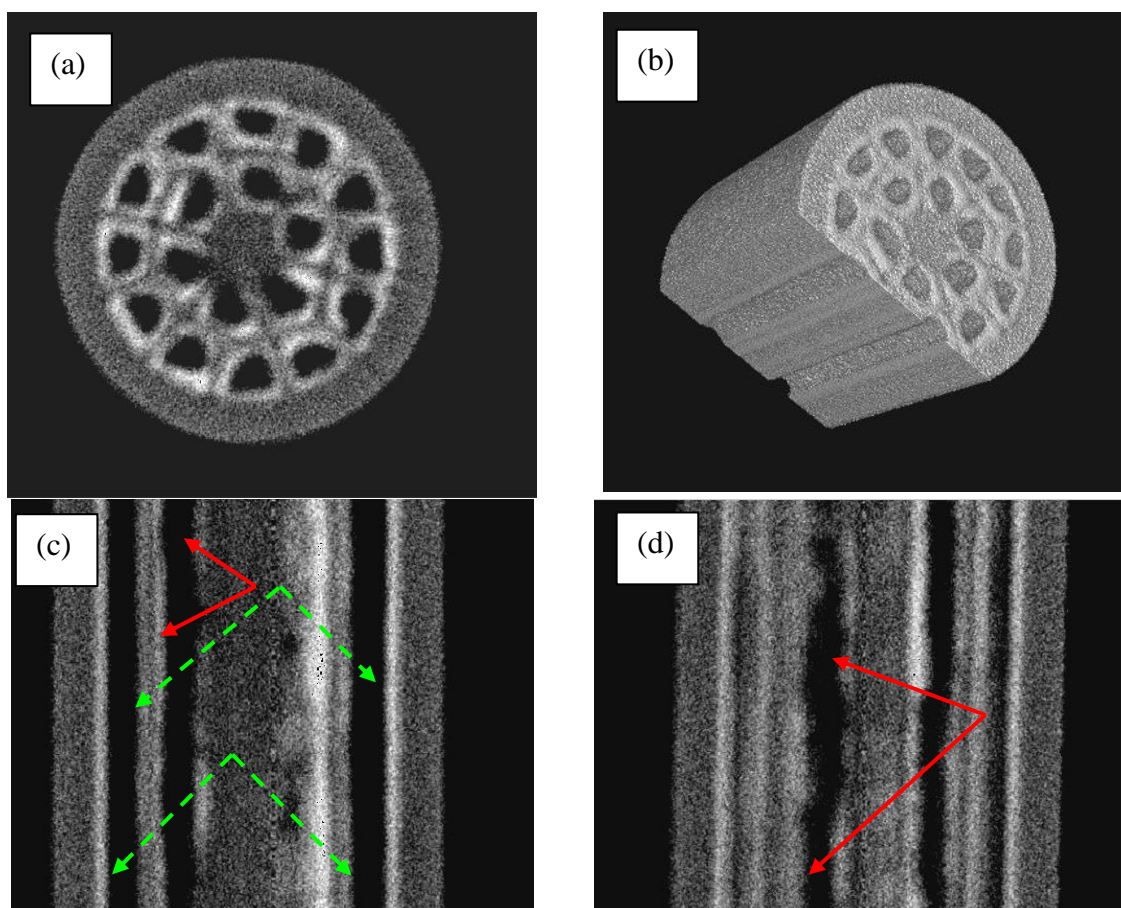


Fig. 10 X-ray microtomography images of the Hypertech MgB_2 wire MB3: a)-axial, b)- 3D reconstruction, c)-sagittal, d) frontal showing non flat interfaces (continuous arrows) and flat ones (interrupted arrows).

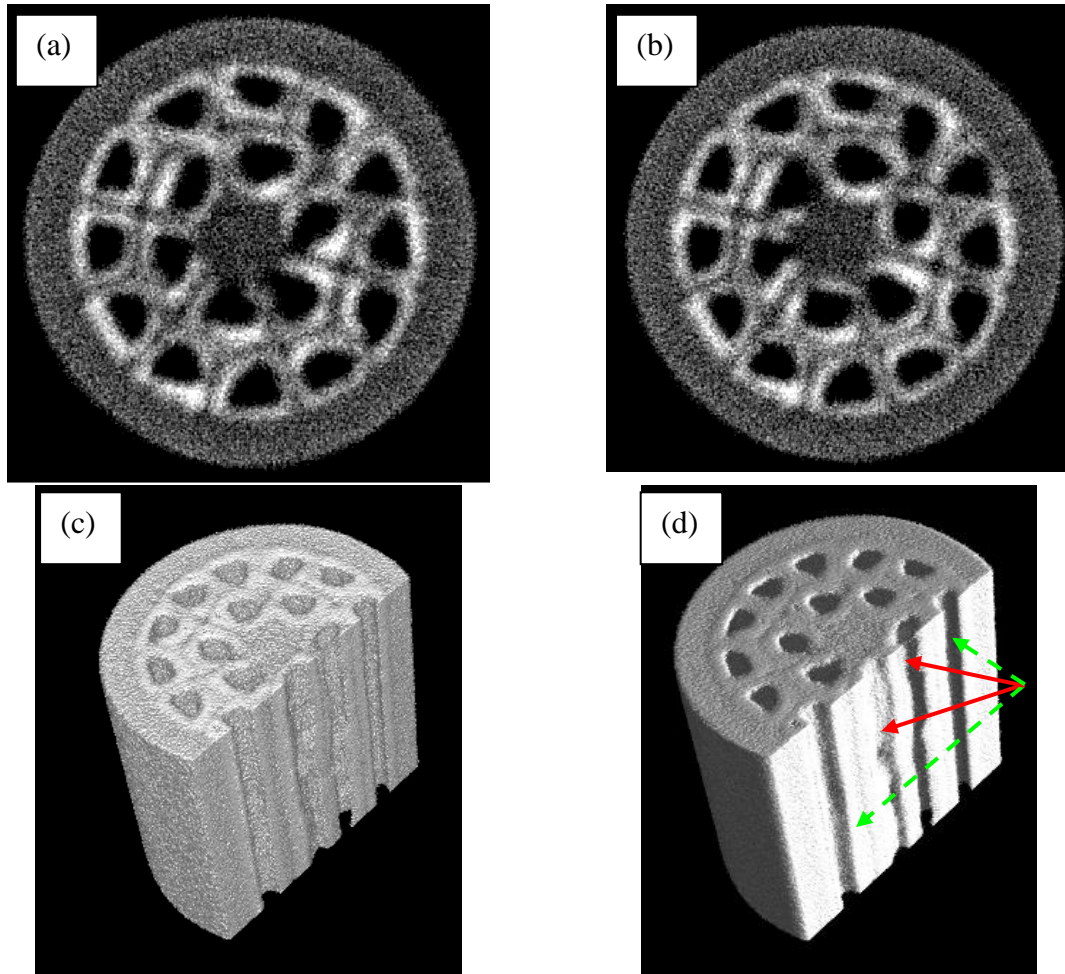


Fig. 11 X-ray microtomography images of the Hypertech MgB_2 wire MB2: a) and b) - axial images taken at different positions, c) and d) - 3D reconstructions for different image processing conditions. Note different geometrical perfection of the superconducting inner and outermost regions (e.g. follow the arrows in d): continuous lines for low geometrical perfection and interrupted for a higher one).

A correlation between superconducting characteristics and the geometrical perfection is proposed. However, further research is necessary to explore it and to determine the criteria and its limitations. One important aspect is the introduction of parameters and methodology to define numerically the *geometrical perfection*. This may help to look and understand in detail the relationship between architecture and superconducting characteristics. It would also be the first step for searching of a mathematical model to define the relationship between geometrical perfection and superconducting characteristics.

4. Conclusion

Commercial wires of MgB_2 produced by HyperTech, with different architecture and subjected to two heat treatments were compared with respect to their superconducting properties of T_c , J_c , H_{lr} , pinning force, macro flux jumps behaviour and their 3D geometrical perfection as revealed by x-ray microtomography. Correlations between processing, superconducting

characteristics and geometrical details are proposed and discussed. It is shown that XRT has several powerful advantages vs. traditional 2D microscopy methods in characterizing superconducting wires such as: (1) XRT is useful for searching relevant hidden macro-defects and observation of their 3D shape; (2) XRT allows visualization of the 3D geometrical integrity and perfection of the components of the composite wires so that determination of some geometrical parameters in a qualitative and in the future quantitative manner is possible; (3) XRT is a non-invasive method and any 3D shapes and surfaces including the 2D ones can be observed. (4) Conventional microscopy operates with 2D surfaces and, to obtain them, time and energy consuming operations (e.g. cutting, polishing) are needed. (5) XRT also has a good potential for in-situ non-destructive characterization of the wires during thermo mechanical processing, or during wires application (e.g. wires winding) and service. (6) XRT opens new possibilities in understanding the relationship between processing, architecture and superconducting characteristics of the

composite wires. This can translate into production of wires with optimized or improved working characteristics.

Acknowledgements

Authors thank Dr. L. Miu and Dr. C.J. Thong for critical reading of the manuscript. This work was performed within Partnership program in the priority domains - PN II, funded by MEN-UEFISCDI, project No. 214/2014 BENZISUPRA.

References

- [1] P. Badica, G. Aldica, T. Craciunescu, I. Tiseanu, Y. Ma, K. Togano, *Supercond. Sci Technol.* **21**, 115017 (2008).
- [2] Homepage of Hypertech Inc, USA:
<http://www.hypertechresearch.com/>.
- [3] J. Horvat, W. K. Yeoh, J. H. Kim, S.X. Dou, *Supercond. Sci Technol.* **21**, 065003 (2008).
- [4] T. Holubek, P. Kovac, S. Talcs, I. Husek, T. Melisek, *Supercond. Sci Technol.* **21**, 065013 (2008)
- [5] C.P. Bean, *Phys. Rev. Lett.*, **8**, 250 (1962).
- [6] I. Tiseanu, T. Craciunescu, N.B. Mandache, *Fusion Engineering and Design* **75**, 1005 (2005).
- [7] I. Tiseanu, E. Tsitrone, A. Kreter, T. Craciunescu, T. Loarer, B. Pegourier, T. Dittmar, X-Ray Micro-Tomography Studies on Carbon Based Composite Materials for Porosity Network Characterization *Fusion Eng. Des.* **86**, 1646 (2011).
- [8] S.X. Dou, S. Soltanian, J. Horvat, X.L. Wang, S.H. Zhou, M. Ionescu, H.K. Liu, P. Munroe, M. Tomsic, *Appl. Phys. Lett.* **81**, 3419 (2002).
- [9] X.X. Xi, X.H. Zeng, A. Sukiasyan, J. Jones, J. Hotchkiss, Yu Zhong, C.O. Brubaker, Liu, Zi-Kui; J. Lettieri, D.G. Schlom, Y.F. Hu, E. Wertz, Qi Li, W. Tian, H.P. Sun, X.Q. Pan *Supercond. Sci. Technol.* **15**, 451 (2002)
- [10] J.W. Ekin, *Supercond. Sci. Technol.* **23**, 083001 (2010).
- [11] W.A. Fietz, W.W. Webb, *Phys. Rev. B* **178**, 657 (1969)
- [12] M. Eisterer; *Supercond. Sci. Technol.* **20**, R47. (2007).
- [13] K. Murai; J. Hori, Y. Fujii, J. Shaver, G. Kozlowski, *Cryogenics* **45**, 415 (2008).
- [14] K. Osamura, S.S. Oh, S. Ochiai, *Supercond. Sci. Technol.* **5**, 1 (1992).

*Corresponding author: badica2003@yahoo.com;